

Enhancing thermoelectric performance in Janus MoTeS through periodic structural alternations and van der Waals contact

Yi-Ming Chen(陈一鸣), Shi-Hua Tan(谭仕华), Xuan-Hao Cao(曹煊浩), and Yan-Hong Zhou(周艳红)
Citation: Chin. Phys. B, 2026, 35 (**7**): 078501. DOI: 10.1088/1674-1056/ae1203
http://cpb.iphy.ac.cn; http://iopscience.iop.org/cpb

What follows is a list of articles you may be interested in

Gate-tunable high-responsivity photodiode based on 2D ambipolar semiconductor

Wentao Yu(于文韬), Long Zhao(赵龙), Yanfei Gao(高延飞), Shiping Gao(高石平), Yuekun Yang(杨悦昆), Chen Pan(潘晨), Shi-Jun Liang(梁世军), and Bin Cheng(程斌)
Chin. Phys. B, 2025, 34 (**1**): 018502. DOI: 10.1088/1674-1056/ad9c44

Recent progress on two-dimensional ferroelectrics: Material systems and device applications

Zhiwei Fan(范芷薇), Jingyuan Qu(渠靖媛), Tao Wang(王涛), Yan Wen(温艳), Ziwen An(安子文), Qitao Jiang(姜琦涛), Wuhong Xue(薛武红), Peng Zhou(周鹏), and Xiaohong Xu(许小红)
Chin. Phys. B, 2023, 32 (**12**): 128508. DOI: 10.1088/1674-1056/ad08a4

Ultra-high photoresponsive photodetector based on ReS_2/SnS_2 heterostructure

Binghui Wang(王冰辉), Yanhui Xing(邢艳辉), Shengyuan Dong(董晟园), Jiahao Li(李嘉豪), Jun Han(韩军), Huayao Tu(涂华垚), Ting Lei(雷挺), Wenxin He(贺雯馨), Baoshun Zhang(张宝顺), and Zhongming Zeng(曾中明)
Chin. Phys. B, 2023, 32 (**9**): 098504. DOI: 10.1088/1674-1056/acd9c0

Graphene-based heterojunction for enhanced photodetectors

Haiting Yao(姚海婷), Xin Guo(郭鑫), Aida Bao(鲍爱达), Haiyang Mao(毛海央),Youchun Ma(马游春), and Xuechao Li(李学超)
Chin. Phys. B, 2022, 31 (**3**): 038501. DOI: 10.1088/1674-1056/ac1b8b

Donor-acceptor conjugated copolymer with high thermoelectric performance: A case study of the oxidation process within chemical doping

Liangjun Chen(陈凉君), Wei Wang(王维), Shengqiang Xiao(肖生强), and Xinfeng Tang(唐新峰)
Chin. Phys. B, 2022, 31 (**2**): 028507. DOI: 10.1088/1674-1056/ac3504

Enhancing thermoelectric performance in Janus MoTeS through periodic structural alternations and van der Waals contact

Yi-Ming Chen(陈一鸣)[1], Shi-Hua Tan(谭仕华)[2], Xuan-Hao Cao(曹煊浩)[3], and Yan-Hong Zhou(周艳红)[1,†]

[1] *College of Science, East China Jiaotong University, Nanchang* 330013, *China*
[2] *Hunan Province Key Laboratory of Materials Surface and Interface Science and Technology, Central South University of Forestry and Technology, Changsha* 410004, *China*
[3] *Hunan Provincial Key Laboratory of Flexible Electronic Materials Genome Engineering, School of Physics and Electronic Science, Changsha University of Science and Technology, Changsha* 410114, *China*

(Received 16 August 2025; revised manuscript received 4 October 2025; accepted manuscript online 11 October 2025)

Atomic-scale structural engineering provides a promising approach to enhance the thermoelectric performance of low-dimensional materials. The two-dimensional Janus MoTeS, with its inherent out-of-plane asymmetry, enables direct modulation of thermoelectric transport properties through tailored periodic S–Te atomic arrangements. Herein, three Janus MoTeS configurations with periodic S–Te atom alternation are constructed in order to realize highly efficient thermoelectric properties by first-principles calculations based on density functional theory. The Seebeck coefficient is enhanced and the phonon thermal conductance is suppressed when the alternation frequency of the structure in the transport direction increases, yielding a figure of merit (ZT) of 1.58 at 300 K in the high-frequency alternating (HFA) structure. Further, the phonon thermal conductance decreases greatly when the HFA monolayer device is extended into a van der Waals heterojunction, resulting in a high ZT of 1.80 at 300 K, which rises to 3.49 at 500 K. These findings highlight the potential of atomic-level alternation engineering for optimizing thermoelectric performance in Janus 2D materials.

Keywords: thermoelectric properties, periodic structural alternations, two-dimensional materials, van der Waals heterostructure

PACS: 85.80.Fi, 73.50.Lw

DOI: 10.1088/1674-1056/ae1203 **CSTR:** 32038.14.CPB.ae1203

1. Introduction

Heat can be converted to electricity directly using thermoelectric materials, which are valuable in waste heat power generation, outdoor portable power supply, etc., and have garnered tremendous research attention due to the current energy and environmental issues.[1–3] The thermoelectric conversion efficiency of a material is described by a dimensionless quality factor, called figure of merit (ZT) with $ZT = S^2\sigma T/(K_e + K_{ph})$. Here, S is the Seebeck coefficient, σ is electrical conductance, K_e is electronic thermal conductance, K_{ph} is phonon thermal conductance, and T is absolute temperature. So to realize high thermoelectric conversion efficiency, the thermoelectric material should have a large Seebeck coefficient S and electronic conductance σ, and a low electrical and phonon thermal conductance (K_e and K_{ph}). However, a high electronic conductance σ is usually accompanied by a high electronic thermal conductance K_e via the Wiedemann–Franz law, and a high Seebeck coefficient S is often accompanied by lower electrical conductance σ.[4,5] So optimizing these transport coefficients simultaneously is tough because they are strongly coupled with each other and cannot independently enhance the thermoelectric performance of a material.[6–8] Fortunately, it has been reported that the Wiedemann–Franz law is not as applicable in nanoscale systems as in bulk materials.[9,10] Consequently, research efforts have increasingly focused on the thermoelectric properties of two-dimensional (2D) materials. In atomically thin monolayers, the power factors can be enhanced by strategic band structure engineering[11–14] and the carrier mobility can be significantly improved via reducing effective mass based on the quantum confinement effect; meanwhile, the phonon scattering can be improved because of the multiscale distribution of interlayer interfaces, grain boundaries, and defects in two-dimensional monolayer materials.[15,16] For instance, Pathak *et al.* demonstrated a high ZT of 1.55 at 865 K in doped SnTe, where a co-doping strategy of Ag and Mg in self-compensated $Sn_{1.03}Te$ effectively reduces the thermal conductance and improves the power factor,[17] and Liu *et al.* reported that in the layered structure of SnSe, point defects are critical tools for precisely regulating carrier concentration and band structure, with the power factor ($S^2\sigma$) increasing from $\sim 8\ \mu W\cdot cm^{-1}\cdot K^{-2}$ to $\sim 31.5\ \mu W\cdot cm^{-1}\cdot K^{-2}$ at 623 K.[18] Jia *et al.* systematically investigated the thermoelectric properties of $MoS_2/MoSe_2$ van der Waals heterostructures and found that the van der Waals heterostructure induces strong localization of electrons and phonons due to interface effects, significantly reducing thermal conductance, with the phonon thermal conductance K_{ph} reduced to ∼5 pW/K at 300 K.[19] Jue Wang *et al.* proposed that monolayer MoS_2–

†Corresponding author. E-mail: yhzhou80@163.com

© 2026 Chinese Physical Society and IOP Publishing Ltd. All rights, including for text and data mining, AI training, and similar technologies, are reserved.

$MoSe_2$ aperiodic superlattices can effectively reduce phonon thermal conductance and reach a ZT of 1.38 at 500 K.[20] Stimulated by the in-plane lateral heterostructure in the application of thermoelectric devices, Song and Sun demonstrated that twist angle engineering in $WSe_2/MoSe_2$ superlattice heterostructures optimizes the carrier concentration and band gap, achieving a peak ZT of 1.35 at 600 K and a twist angle of 21.79° due to enhanced power factor and reduced thermal conductance.[21]

Janus transition metal dichalcogenides (TMDs), a distinctive class of two-dimensional (2D) materials characterized by out-of-plane structural symmetry breaking arising from the composition of each layer with distinct elements differing in atomic radius, electronegativity, and atomic mass, demonstrate a favorable combination of relatively high electrical transport efficiency and low K_{ph}, which exhibits significant promise for thermoelectric applications.[22–28] Zhang *et al.* demonstrated that Janus materials with their atomic mass differences can greatly optimize phonon scattering,[22] and Patel *et al.* demonstrated that the Janus WSTe monolayer exhibits ultralow K_{ph}, which is nearly 150 times smaller than WS_2 and 100 times smaller than WSSe near room temperature due to out-of-plane structural asymmetry disrupting phonon dispersion, and concurrently, its Seebeck coefficient S reaches 322 μV/K owing to asymmetric band structures, yielding a high ZT of 2.56 at 1200 K.[23] Xiong *et al.* further introduced disorder through atomic positional tuning and achieved significant thermoelectric improvements in Janus MoSSe. They found the atomic disorder in Janus MoSSe induces local atomic-level resonance, increases the electronic density of states and improves S, and simultaneously decreases K_{ph}.[25] So local structural tuning at the atomic scale is an effective means to obtain high thermoelectric performance.

Compared to the Janus MoSSe monolayer and WSTe monolayer,[24,26] the Janus MoTeS monolayer shows a more significant difference in atomic radius and mass between the Te and S layers, which may result in stronger phonon scattering. Here, we further study this atomic-scale tuning method of the effect of periodic alternation of intrinsic elements on electronic and phonon transport, aiming to realize high thermoelectric performance in MoTeS constructed devices. In the work, first-principles are implemented to explore the thermoelectric performance of Janus MoTeS, mainly focusing on the high-frequency (S/Te) alternations and van der Waals heterojunctions to enhance ZT. It is shown that increasing the alternation frequency in the transport direction can enhance the Seebeck coefficient S and simultaneously suppress the phonon thermal conductance K_{ph}, yielding ZT of 1.58 at 300 K in the high-frequency alternating (HFA) structure. Further, the phonon thermal conductance K_{ph} decreases greatly when the HFA monolayer device is extended into a van der Waals heterojunction, resulting in a high ZT of 1.80 at 300 K, which rises to 3.49 at 500 K. This work is useful in designing high-performance thermoelectric materials via periodic structural alternations.

2. Calculation details

The thermoelectric transport properties are calculated using density functional theory (DFT) combined with the non-equilibrium Green's function (NEGF) method, and calculations are performed with the Atomistix ToolKit package.[29,30] The generalized gradient approximation (GGA) and Perdew–Burke–Ernzerhof (PBE) are used to describe the exchange–correlation potential of electrons.[31] Before calculations of the transport properties, all device structures are fully optimized, with a convergence criterion for structural relaxation set at a force on each atom less than 0.02 eV·Å^{-1}. The double-zeta polarized (DZP) basis set is employed to describe the localized atomic orbitals.[32,33] The cut-off energy for the real-space grid is set at 85 Hartree. The convergence criterion for the total energy is set to 10^{-5} Hartree. The electronic temperature is set at 300 K. Periodic boundary conditions are applied in the x direction to eliminate the influence of edges, and a vacuum layer with a thickness of 15 Å is used in the y direction to avoid interactions. The DFT-D2 empirical correction approach is utilized to accurately model the physical attributes of layered materials characterized by weak van der Waals (vdW) interactions.[34]

The electronic transmission spectrum $T_e(\varepsilon)$ is calculated by using the NEGF method. Based on the Caroli formula, the electronic transmission can be given as[35]

$$T_e(\varepsilon) = \mathrm{Tr}\left[G^r_{CC}(\varepsilon)\Gamma^L(\varepsilon)G^\alpha_{CC}(\varepsilon)\Gamma^R(\varepsilon)\right]. \tag{1}$$

Then, the electronic conductance (σ), Seebeck coefficient (S), and electronic thermal conductance (K_e) as functions of the chemical potential can be expressed as follows:[36,37]

$$\sigma(\mu) = e^2 L_0(\mu, T), \tag{2}$$

$$S(\mu, T) = \frac{1}{eT}\frac{L_1(\mu, T)}{L_0(\mu, T)}, \tag{3}$$

$$K_e(\mu, T) = \frac{1}{T}\left[L_2(\mu, T) - \frac{L_1^2(\mu, T)}{L_0(\mu, T)}\right]. \tag{4}$$

The Lorenz function can be represented as

$$L_n(\mu, T) = \frac{2}{h}\int_{-\infty}^{\infty} T_e(E)(E-\mu)^n \frac{-\partial f(E, \mu, T)}{\partial E}\mathrm{d}E, \tag{5}$$

where $f(E, \mu, T)$ is the Fermi–Dirac distribution (a function of E, temperature T and chemical potential μ). The phonon transmission function $T_{ph}(\omega)$ is given by a Caroli type formula, where ω is the phonon frequency. The phonon transmission function is

$$T_{ph}(\omega) = \mathrm{Tr}\left[G^r_C \Gamma_L G^\alpha_C \Gamma_R\right]. \tag{6}$$

In this case, the phononic contribution to thermal conductance ($K_{\rm ph}$) is calculated using the methodology outlined in Ref. [38] with the governing equation[39]

$$K_{\rm ph} = \frac{1}{h}\int_0^{\infty} \frac{{\rm d}\omega}{2\pi}\hbar\omega T_{\rm ph}(\omega)\frac{\partial f_{\rm BE}(\omega,T)}{\partial T}, \tag{7}$$

where $f_{\rm BE}(\omega,T)$ is the Bose–Einstein distribution function, T is the average temperature of the whole device and ω stands for the phonon frequency. The electronic thermal conductance $K_{\rm e}$ is calculated directly from the electron transmission spectrum using Eq. (4).

3. Results and discussion

3.1. Influence of alternation frequency on thermoelectric performance

In order to study the effect of periodic alternation of the intrinsic elements S and Te on the thermoelectric performance, three configurations are constructed based on the two-dimensional material MoTeS, including the low-frequency alternating (LFA) structure, the high-frequency alternating (HFA) structure, and the pristine monolayer structure for comparison, as shown in Fig. 1. Each device consists of three regions: the left and right electrodes and a central scattering region. The pristine Janus structure, as shown in Fig. 1(a), features sulfur (S) and tellurium (Te) atoms positioned on opposing top and bottom surfaces. The LFA structure, depicted in Fig. 1(b), exhibits a periodic alternation of S and Te atoms along the transport direction with a period of two unit cells; as highlighted in the blue box, within one period, half of the adjacent S atoms on the top surface are substituted with Te atoms, and S atoms occupy corresponding positions on the bottom surface. The HFA structure, shown in Fig. 1(c), has a period of one unit cell, with a surface atomic arrangement similar to the LFA but higher-frequency alternation than the LFA.

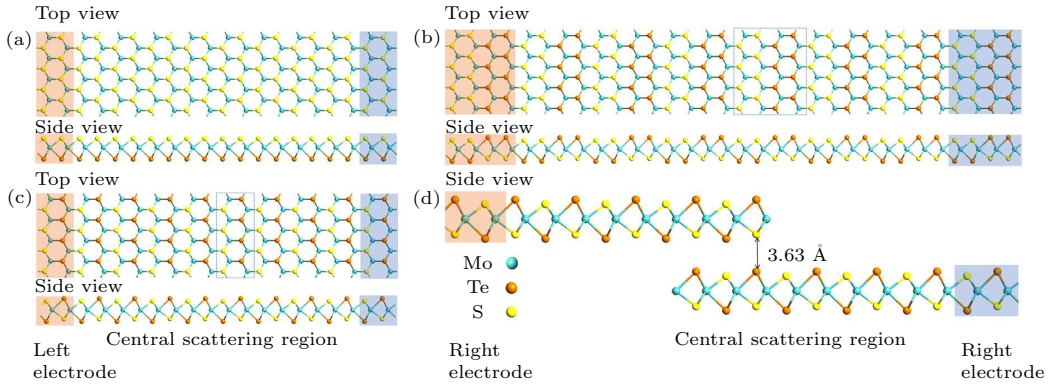


Fig. 1. (a)–(c) Top and side views of three MoTeS configurations with different period S–Te atom alternation frequencies along the transport direction: (a) the MoTeS pristine structure with no alternation of S and Se where the top surface consists of S atoms and the bottom surface consists of Te atoms, (b) the LFA structure owning a low S–Te atom alternation frequency with a period of two unit cells, (c) the HFA structure deserving a high-frequency alternation with a period of one unit cell. (d) The side view of a van der Waals bilayer device constructed from two HFA monolayers.

The temperature dependence of phonon thermal conductance $K_{\rm ph}$ for the three configurations is illustrated in Fig. 2(a). The $K_{\rm ph}$ for all three configurations rises rapidly as the temperature increases at the beginning and then nearly stabilizes when the temperature is beyond 300 K. However, a significantly lower $K_{\rm ph}$ is observed in the LFA structure as compared to pristine MoTeS, attributed to the periodic structural alternation. This reduction in $K_{\rm ph}$ is further enhanced in the HFA structure, resulting from further enhanced phonon-interface scattering. Specifically, the phonon thermal conductance $K_{\rm ph}$ for the HFA structure is reduced to 67% of that for the pristine MoTeS structure. According to the formula of the phonon thermal conductance,[39] the total phonon transmission $T_{\rm ph}$ makes a great contribution to the phonon thermal conductance. It can be seen from Fig. 2(b) that marked suppression of phonon transmission is observed in the LFA and HFA structures relative to the pristine structure, nearly over all phonon frequencies except near 35 meV and 20 meV. The transmission coefficients for the HFA structure at low-frequency phonons near the energy 12 meV and the energy ranges 22–32 meV decrease much more significantly as compared to those for the LFA structure, which results in the lowest phonon thermal conductance $K_{\rm ph}$ in the HFA structure.

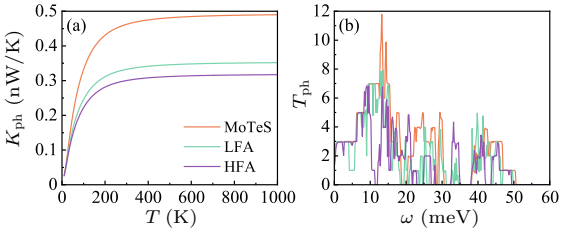


Fig. 2. (a) The temperature-dependent phonon thermal conductance $K_{\rm ph}$ and (b) phonon transmission spectrum $T_{\rm ph}$ for the three different alternation frequency structures of pristine MoTeS, LFA and HFA.

To demonstrate the specific contributions of different phonon modes to phonon transmission, the calculated local phonon density of states (LPDOS) for them is presented in Fig. 3. The phonon density of states of the pristine structure has values over the whole range of phonon frequencies except near 35 meV and 20 meV as shown in Fig. 3(b), which

means that phonons in the left electrode can transmit through the central region and reach the right electrode easily, leading to the high phonon transmission as shown in Fig. 2(b). Moreover, its large values are mainly concentrated in the energy ranges 10–18 meV and 22–32 meV, which induces higher K_{ph} due to the dominance of low-frequency phonons in heat transfer.[40] As shown in Fig. 3(b), LFA exhibits a reduction in LPDOS within the 22–32 meV range. This suppression is directly attributed to periodic defects, which simultaneously block phonon propagation at these specific energies and enhance phonon scattering.[41,42] This effect is further amplified in HFA as shown in Fig. 3(c), which exhibits significantly stronger suppression of the phonon density of states within the 22–32 meV range than that in LFA, resulting in substantially reduced T_{ph} and K_{ph}. Notably, as the frequency of periodic alternation defects increases, phonon transport becomes progressively impeded.

The distribution of local phonon density of states (LPDOS) projected along the z-direction is presented for (a) pristine MoTeS, (b) LFA, and (c) HFA configurations. The color scale indicates the magnitude of the LPDOS at each spatial point and frequency.

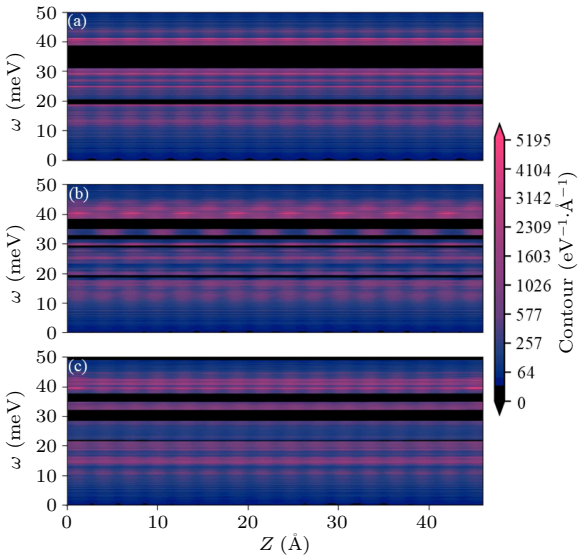


Fig. 3. The distribution of local phonon density of states (LPDOS) projected along the z-direction for (a) pristine MoTeS, (b) LFA, and (c) HFA configurations. The color scale indicates the magnitude of the LPDOS at each spatial point and frequency.

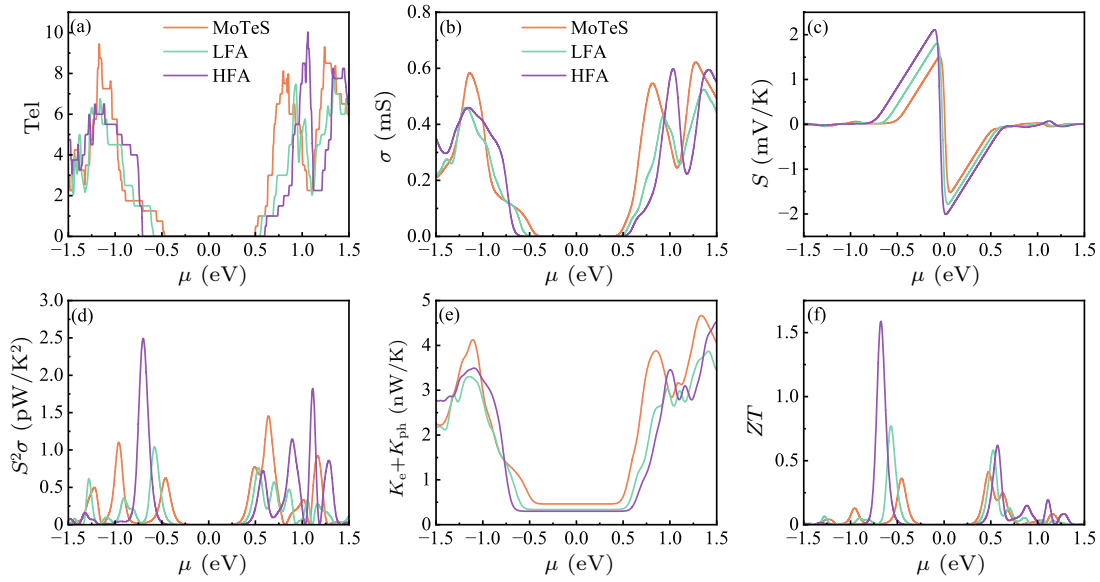


Fig. 4. (a) Electron transmission spectrum, and (b)–(f) the conductance, Seebeck coefficient, power factor, total thermal conductance, and ZT value as a function of chemical potential for the structures of the pristine MoTeS, LFA and HFA, respectively. The temperature is set at 300 K.

Subsequently, the electronic transport and thermoelectric performance of pristine MoTeS, LFA, and HFA structures are investigated. As shown in Fig. 4(a), at most electron energies, the electron transmission for the pristine structure has the highest values among the three configurations. This superior transmission originates from its uniform Janus configuration, where sulfur (S) and tellurium (Te) atoms arrange on opposing surfaces, minimizing electron scattering. However, at electron energies from about -1 eV to -0.73 eV, the electron transmission for HFA is greatly enhanced, much higher than that for the pristine structure, which leads to improved electrical conductance as shown in Fig. 4(b). Figure 4(c) displays the Seebeck coefficient as a function of chemical potential. HFA exhibits higher S values than LFA, and pristine MoTeS exhibits μ values in the range from about -0.8 eV to -0.2 eV due to its highly alternating structure. Then the power factor $PF = S^2\sigma$, a key metric for device thermoelectric performance, reaches its maximum value of 2.46 pW/K^2 at $\mu = -0.73$ eV for HFA in Fig. 4(d). The total thermal conductance, comprising electronic and phononic contributions, is presented in Fig. 4(e). The trend in K_e mirrors electrical conductance as shown in Fig. 4(b), confirming their positive correlation. Critically, HFA demonstrates consistently lower K_{total} near $\mu = -0.73$ eV compared to LFA and pristine MoTeS, pri-

marily due to the reduced K_{ph}. Finally, a maximum ZT value of 1.58 for the HFA structure is achieved, much larger than that for the pristine structure (0.43) and LFA (0.77), as shown in Fig. 4(f). This superior ZT in HFA stems from the significant increase in PF and simultaneous suppression of K_{ph}.

3.2. Influence of weak coupling interfaces on thermoelectric performance

In order to further improve the thermoelectric properties of Janus MoTeS devices via suppressing K_{ph} deeply, the vdW-HFA heterojunction is constructed with two HFA monolayers stacked via a weak van der Waals junction, as shown in Fig. 1(d). The interlayer contact contains three unit cells, and the interlayer spacing is 3.63 Å in the vdW-HFA heterojunction. The temperature-dependent K_{ph} and corresponding transmission spectra $T_{ph}(\omega)$ are presented in Fig. 5. Attributed to enhanced interface scattering, the phonon transmission below 50 meV for vdW-HFA is more deeply suppressed than that for HFA, as shown in Fig. 5(b), accompanied by a substantially lower K_{ph} for vdW-HFA compared with that for HFA, as observed in Fig. 5(a).

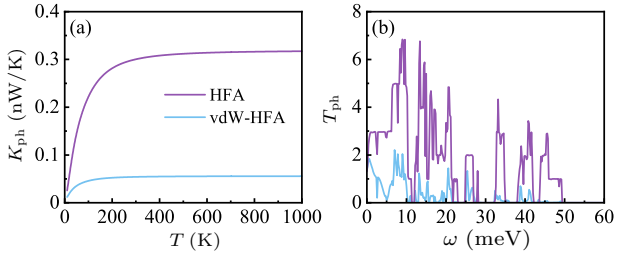


Fig. 5. (a) The temperature-dependent phonon thermal conductance and (b) the phonon transmission spectrum for the HFA and vdW-HFA, respectively.

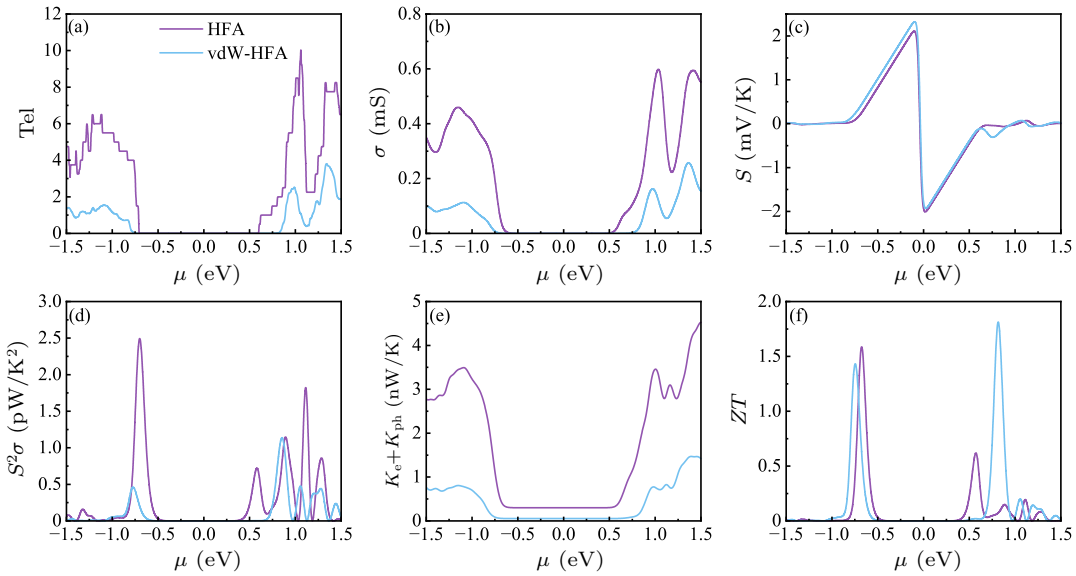


Fig. 6. (a) Electron transmission spectrum, and (b)–(f) the conductance, Seebeck coefficient, power factor, total thermal conductance, and ZT value as a function of chemical potential for the structures of the pristine MoTeS, LFA and HFA, respectively. The temperature is set at 300 K.

The electronic transport and thermoelectric properties for the vdW-HFA structure are shown in Fig. 6 (also presented is that for HFA for comparison). Compared with that for HFA, the electron transmission coefficient for vdW-HFA is also greatly reduced (see Fig. 6(a)) because the weak interlayer coupling in the vdW structure constrains the available transmission channels and hampers the electron tunneling during interlayer propagation (the corresponding analysis will be given later). As a result, the electrical conductance of vdW-HFA is also diminished compared with that of HFA, as can be seen from Fig. 6(b). The S for vdW-HFA is marginally higher than that for HFA, as shown in Fig. 6(c), which is inversely correlated with its reduced electrical conductance (see Fig. 6(c)). The maximum power factors PF for HFA and vdW-HFA occur at the chemical potentials μ of -0.68 eV and 0.81 eV, respectively, with the maximum PF for HFA being approximately twice that of vdW-HFA, as illustrated in Fig. 6(d). This disparity stems from the electrical conductance for vdW-HFA being much lower than that for HFA. The total thermal conductance K_{tot} of vdW-HFA is substantially lower than that of HFA, as shown in Fig. 6(e), due to the reductions in both K_e and K_{ph}. Although the electron conductance in vdW-HFA is also suppressed greatly, a significantly enhanced figure of merit ZT 1.80 at 300 K is obtained for vdW-HFA (higher than the ZT_{max} 1.58 for HFA) through pronounced suppression of K_{tot} via weak interlayer coupling, which prevails over the competing effect of $S^2\sigma$, as demonstrated in Fig. 6(f).

To give the physical reason why the transmission coefficient and conductance for vdW-HFA are more greatly reduced compared with those for HFA, the local device density of states (LDDOS) for both structures is calculated at the corresponding chemical potentials -0.68 eV for HFA and 0.81 eV for vdW-HFA. As can be seen from Fig. 7, the LDDOS for HFA is distributed on the whole device, so electrons can trans-

mit through easily, resulting in the rather high transmission coefficient and conductance, whereas in the vdW-HFA, it remains highly localized and confined, which makes it hard for electrons to traverse the van der Waals interface, leading to the smaller transmission coefficient and conductance. Similar analysis can also be applied to the K_e difference between the HFA and vdW-HFA.

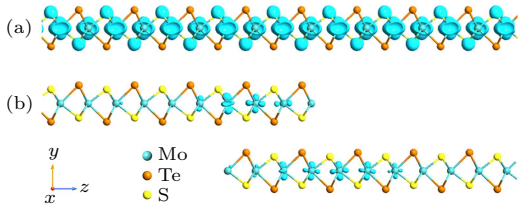


Fig. 7. The distribution of local device density of states for (a) the HFA at the chemical potential of −0.68 eV and (b) the vdW-HFA at 0.81 eV.

The maximum ZT_{max} values for both HFA and vdW-HFA increase with the increase of temperature within the considered temperature range from 100 K to 500 K, as shown in Fig. 8. A pronounced temperature-dependent enhancement of the ZT_{max} value for vdW-HFA is observed, surpassing that for HFA at approximately 200 K. Beyond 200 K, the substantial reduction in K_{ph} for vdW-HFA prevails over the lower PF, resulting in a higher ZT relative to HFA. What is more, the maximum ZT_{max} value for vdW-HFA rises to 3.49 as the temperature increases to 500 K. Then, how does the temperature increase lead to the enhancement of ZT from 1.80 to 3.49? As can be seen from Table 1, the significant enhancement of ZT_{max} from 1.80 at 300 K to 3.49 at 500 K is primarily driven by the synergistic effects of temperature on the thermoelectric parameters: the Seebeck coefficient S increases markedly from 0.24 mV/K to 0.31 mV/K, resulting in a substantial 58% improvement in the power factor ($S^2\sigma$) from 0.79 pW/K^2 to 1.25 pW/K^2 though the electrical conductivity σ experiences a slight decrease from 13.69 μS to approximately 12.98 μS. In addition, the total thermal conductivity K_{tot} is nearly stable as the phonon thermal conductivity K_{ph} and the electronic thermal conductivity K_e remain nearly unchanged. The temperature T in the numerator of the ZT expression acts as a linear amplifier, and its increase from 300 K to 500 K (a 67% rise) directly magnifies the gain in ($S^2\sigma T$). The overall growth of the numerator ($S^2\sigma$) by 163% vastly outweighs the minimal change in the denominator (K_{tot}), thereby dominating the enhancement of ZT and demonstrating the outstanding high-temperature thermoelectric performance of the vdW-HFA junction.

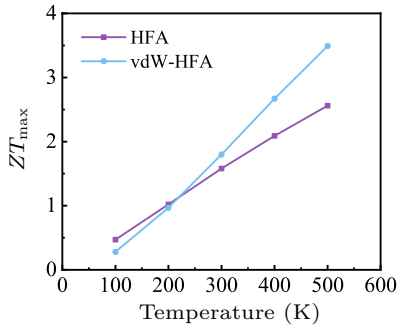


Fig. 8. The ZT_{max} as a function of temperature for the HFA and vdW-HFA. The ZT_{max} values are obtained by optimizing the chemical potential at each temperature point.

Table 1. Summary of the electrical conductance (σ), Seebeck coefficient (S), power factor ($S^2\sigma$), electron thermal conductance (K_e), phonon thermal conductance (K_{ph}), and figure of merit (ZT) for all the structures at 300 K, and for the vdW-HFA at 500 K.

	μ (eV)	σ (μS)	S (mV/K)	$S^2\sigma$ (pW/K^2)	K_e (nW/K)	K_{ph} (nW/K)	ZT
MoTeS	0.48	18.92	0.21	0.83	0.09	0.46	0.43
LFA	–0.56	16.93	0.22	0.82	0.05	0.33	0.63
HFA	–0.68	40.05	0.24	2.31	0.14	0.30	1.58
vdW-HFA	0.81	13.69	0.24	0.79	0.08	0.05	1.80
vdW-HFA (500 K)	0.79	12.98	0.31	1.25	0.08	0.06	3.49

4. Conclusion

In summary, the thermoelectric performance of Janus MoTeS-based devices were studied by first-principles calculations based on density functional theory. Firstly, we investigated the impact of period S–Te atom alternation frequency on the thermoelectric performance of Janus MoTeS-based devices, as the two-dimensional Janus MoTeS has inherent out-of-plane asymmetry. Among the three configurations with different alternation frequencies, the HFA structure demonstrated superior thermoelectric performance as the Seebeck coefficient was enhanced and the phonon thermal conductance was suppressed simultaneously when the alternation frequency of the structure in the transport direction increased. A maximum ZT of 1.58 was obtained in the HFA structure at 300 K. Then, in order to further improve the thermoelectric properties of Janus MoTeS devices via suppressing K_{ph} deeply, the vdW-HFA heterojunction was constructed with two HFA monolayers stacked via a weak van der Waals junction. Indeed, the phonon thermal conductance decreased greatly, resulting in a high ZT of 1.80 at 300 K, which rose to 3.49 as the temperature increased to 500 K, and in experiments, techniques such as stepwise growth processes have demonstrated the feasibility of creating atomically sharp interfaces within layered materials. The results suggest that atomic-level structural design plays an important role in modulating the thermoelectric properties of Janus 2D materials, which is useful for further exploration of their device applications.

Acknowledgement

Project supported by the National Natural Science Foundation of China (Grant No. 12264014).

References

[1] Bell L E 2008 *Science* **321** 1457
[2] DiSalvo F J 1999 *Science* **285** 703
[3] Ghosh T, Dutta M, Sarkar D and Biswas K 2022 *J. Am. Chem. Soc.* **144** 10099
[4] Dresselhaus M S, Chen G, Tang M Y, Yang R, Lee H, Wang D, Ren Z, Fleurial J P and Gogna P 2007 *Adv. Mater.* **19** 1043
[5] Mahan G and Sofo J 1996 *Proc. Natl. Acad. Sci. USA* **93** 7436
[6] Jia P Z, Xie J P, Deng Y X, Zhang Y, Wang H B, Liao G H, Yu X and Xie Z X 2023 *Diamond and Related Materials* **137** 110103
[7] Zhang X and Pei Y 2017 *npj Quantum Materials* **2** 68
[8] Yang L, Gordon M P, Menon A K, Bruefach A, Haas K, Scott M, Prasher R S and Urban J J 2021 *Science Advances* **7** 6000
[9] Kubala B, König J and Pekola J 2008 *Phys. Rev. Lett.* **100** 066801
[10] Murphy P, Mukerjee S and Moore J 2008 *Phys. Rev. B* **78** 161406
[11] Novoselov K S, Geim A K, Morozov S V, Jiang D E, Zhang Y, Dubonos S V, Grigorieva I V and Firsov A A 2004 *Science* **306** 666
[12] Mak K F, Lee C, Hone J, Shan J and Heinz T F 2010 *Phys. Rev. Lett.* **105** 136805
[13] Palacios-Berraquero C, Kara D M, Montblanch A R P, Barbone M, Latawiec P, Yoon D, Ott A K, Loncar M, Ferrari A C and Atatüre M 2017 *Nat. Commun.* **8** 15093
[14] Ramalingam G, Kathirgamanathan P, Ravi G, Elangovan T, Arjun kumar B, Manivannan N and Kasinathan K 2020 *Quantum Dots - Fundamental and Applications* (London: IntechOpen) pp. 11–16
[15] Hu W and Yang J 2017 *Journal of Materials Chemistry C* **5** 12289
[16] Xia W, Dai L, Yu P, Tong X, Song W, Zhang G and Wang Z 2017 *Nanoscale* **9** 4324
[17] Pathak R, Sarkar D and Biswas K 2021 *Angewandte Chemie International Edition* **60** 17686
[18] Liu D, Wang D, Hong T, Wang Z, Wang Y, Qin Y, Su L, Yang T, Gao X and Ge Z, *et al*. 2023 *Science* **380** 841
[19] Jia P Z, Zeng Y J, Wu D, Pan H, Cao X H, Zhou W X, Xie Z X, Zhang J X and Chen K Q 2019 *J. Phys.: Condens. Matter* **32** 055302
[20] Wang J, Cao X H, Zeng Y J, Luo N N, Tang L M and Chen K Q 2023 *Applied Surface Science* **612** 155914
[21] Song J and Sun M 2024 *ACS Applied Materials & Interfaces* **16** 3325
[22] Zhang Z, Xie Y, Peng Q and Chen Y 2016 *Scientific Reports* **6** 21639
[23] Patel A, Singh D, Sonvane Y, Thakor P and Ahuja R 2020 *ACS Applied Materials & Interfaces* **12** 46212
[24] Lin Y Q, Yang Q, Wang Z Q, Geng H Y and Cheng Y 2023 *Phys. Chem. Chem. Phys.* **25** 31312
[25] Xiong H, Nie X, Deng S and Zhao L 2024 *ACS Applied Materials & Interfaces* **16** 70839
[26] Shang Y, Pan X, Jia Y, Wu Y and Sun M 2025 *Nanoscale* **17** 13861
[27] Tang Z, Wang X, He C, Li J, Chen M, Tang C and Ouyang T 2024 *Phys. Rev. B* **110** 134320
[28] Wang X, Tang Z, Li J, He C, Chen M, Tang C and Ouyang T 2025 *Phys. Rev. B* **111** 104316
[29] Brandbyge M, Mozos J L, Ordejón P, Taylor J and Stokbro K 2002 *Phys. Rev. B* **65** 165401
[30] Taylor J, Guo H and Wang J 2001 *Phys. Rev. B* **63** 245407
[31] Perdew J P, Burke K and Ernzerhof M 1996 *Phys. Rev. Lett.* **77** 3865
[32] Cai Y, Lan J, Zhang G and Zhang Y W 2014 *Phys. Rev. B* **89** 035438
[33] Wu D, Cao X H, Jia P Z, Zeng Y J, Feng Y X, Tang L M, Zhou W X and Chen K Q 2020 *Science China Physics* **63** 276811
[34] Lee K, Murray E D, Kong L, Lundqvist B I, Langreth D C 2010 *Phys. Rev. B* **82** 081101
[35] Meir Y and Wingreen N S 1992 *Phys. Rev. Lett.* **68** 2512
[36] Nozaki D, Sevincli H, Li W, Gutiérrez R and Cuniberti G 2010 *Phys. Rev. B* **81** 235406
[37] Joachim C, Gimzewski J K and Aviram A 2000 *Nature* **408** 541
[38] Xie Z X, Tang L M, Pan C N, Li K M, Chen K Q and Duan W 2012 *Appl. Phys. Lett.* **100** 073105
[39] Yamamoto T and Watanabe K 2006 *Phys. Rev. Lett.* **96** 255503
[40] Qian X, Zhou J and Chen G 2021 *Nat. Mater.* **20** 1188
[41] Osborn R, Goremychkin E, Kolesnikov A and Hinks D 2001 *Phys. Rev. Lett.* **87** 017005
[42] Ghosh K, Kusiak A and Battaglia J L 2023 *Phys. Rev. B* **108** 214309